

Photovoltaic neurointerface based on aluminum antimonide nanocrystals

Mertcan Han  ^{1,6}, Houman Bahmani Jalali  ^{2,5,6}, Erdost Yildiz  ³, Mohammad Haroon Qureshi  ³, Afsun Şahin ^{3,4} & Sedat Nizamoglu  ^{1,2}✉

Light activated modulation of neural activity is an emerging field for the basic investigation of neural systems and development of new therapeutic methods such as artificial retina. Colloidal inorganic nanocrystals have great potential for neural interfaces due to their adjustable optoelectronic properties via high-level structural, compositional, and size control. However, toxic heavy metal content (e.g., cadmium, mercury), electrochemical coupling to the cells and low photon-to-current efficiency limit their effective use. Here, we introduce the use of aluminum antimonide (AlSb) nanocrystals as the cell interfacing layer for capacitive neural stimulation in the blue spectrum. We demonstrate successful photostimulation of primary hippocampal neurons below ocular safety limits. In addition, our device shows high biocompatibility in vitro and passive accelerated ageing tests indicate a functional lifetime over 3 years showing their feasible use for chronic implants. We demonstrate that nanocrystal biointerfaces hold high promise for future bioelectronics and prostheses.

¹ Department of Electrical and Electronics Engineering, Koç University, Istanbul, Turkey. ² Graduate School of Biomedical Science and Engineering, Koç University, Istanbul, Turkey. ³ Koç University Research Center for Translational Medicine, Koç University, Istanbul, Turkey. ⁴ Department of Ophthalmology, Medical School Koç University, Istanbul, Turkey. ⁵ Present address: Photonic Nanomaterials group, Istituto Italiano di Tecnologia, Genova, Italy. ⁶ These authors contributed equally: Mertcan Han, Houman Bahmani Jalali. ✉email: snizamoglu@ku.edu.tr

Neuronal stimulation is the fundamental method to communicate with the living systems allowing the treatment of nervous-system disorders and understanding the neuronal circuitry in the brain¹. Nanomaterials represent unique structural, electrical, and optical features to be used as the mediators of neuronal stimulation by transforming primary stimulus to spatiotemporally confined secondary stimulus². Among a wide variety of nanomaterials, colloidal inorganic semiconductor nanocrystals (NCs) offer a unique platform due to their strong absorption, high stability, and adjustable optoelectronic properties that can be sensitively tuned by modifying their size, shape, and composition³⁻⁵. Moreover, they allow for low cost, low temperature, and solution-based fabrication of devices^{6,7}.

There are fundamental challenges that need to be addressed simultaneously for proper neurointerfacing via nanocrystals. (1) So far, most of the efforts were concentrated on cadmium (Cd) and mercury (Hg) based nanocrystals^{3,8,9}, but they may be hazardous due to the binding of toxic heavy-metal-ions to the mitochondrial proteins in the biological systems¹⁰. Hence, toxic heavy metal free NCs are preferable. (2) The use of toxic nanocrystals can also necessitate to coat with additional layers for cell attachment and increase of current levels, which can undesirably vary the coupling mechanism of the biointerface with the cells³. (3) The stimulation mechanism needs to be based on the safe mechanisms that do not induce adverse effects on cells. Neural interfaces based on heavy-metal-free indium phosphide (InP) NCs have been used and facilitate optical neural stimulation of a single cell by electrochemical charge transfer^{11,12}. Faradaic charge injection may also cause oxidation and reduction reactions on the surface of the biointerface, which reduce device performance over time¹³. Moreover, depending on the reactions, these charge-transfer processes may also change the ion and pH levels in the medium that might be detrimental to the cells¹³. Even though Faradaic stimulation can be safely used at controlled levels, which can be balanced by the living systems^{11,12,14}, capacitive stimulation based on the charging and discharging of an electrical double layer without any electrochemical reaction is the gold standard for safe neural stimulation without introducing any harmful side products to the cellular environment¹⁵⁻²⁰. (4) The optoelectronic stability of NCs in biological environment is also critical. For example, perovskite NCs suffer from low stability in aqueous environment and even ambient atmospheric conditions, which limit their use for interfacing with biological systems²¹⁻²³. (5) It is also another important challenge to generate sufficiently high levels of charging for photostimulation at moderate light intensity levels. For example, although the generated current can lead to an average depolarization of 2.3 mV under 800 mW cm⁻² illumination³, the improvement of depolarization level at lower light intensity level can induce a more efficient nano-biojunction that can operate under low light intensities. Hence, the quest for finding novel nanocrystals that can simultaneously satisfy the above needs are continuing.

In the context of this nanomaterial search, we recently introduced a new member to the colloidal nanocrystal family, aluminum antimonide (AlSb) NCs²⁴. AlSb is a less studied member of the III-V semiconductor family due to its difficult process of bulk crystal growth²⁵. Thus far, it has been prepared with high temperature physical methods²⁶⁻²⁸ for near-infrared optoelectronic devices²⁹, quantum cascade lasers (QCLs)²⁶, and high-speed field-effect transistors (FETs)³⁰. Instead of physical techniques, we synthesized size-tunable colloidal AlSb NCs via a controlled organometallic synthetic route²⁴, which provides the advantage of solution-processability and adaptability for device fabrication.

Herein, we report AlSb nanocrystal based neural interfaces that can simultaneously meet the above requirements and effectively stimulate primary hippocampal neurons (Fig. 1a). We utilize AlSb

NCs as the interfacing layer with the biological medium and they are coupled with poly(3-hexylthiophene) (P3HT) leading to a Type II heterojunction with the P3HT polymer for exciton dissociation (Fig. 1b). The biointerface reveals a fast photoresponse of ~55 μs for high speed photostimulation with a peak capacitive current over 600 μA cm⁻² and capacitive charge injection capacity of 0.19 μC cm⁻² under 445 nm, 100 mW cm⁻² illumination. Furthermore, the biointerface offers high stability after low temperature hydrogen peroxide plasma sterilization, followed by an extensive operational lifetime of more than 36 months proven by passive accelerated ageing tests. Our results point out that AlSb nanocrystals can meet the charge transport requirements of safe and high-performance electrical cellular interfacing.

Results

Preparation and characterization of AlSb NCs. Colloidal AlSb NCs were synthesized by reacting aluminum chloride and antimony bis(trimethylsilyl)amide in the presence of superhydride²⁴ (see Method Section for detailed synthesis procedure). The synthesized AlSb NCs having cubic AlSb structures according to the X-ray diffraction (XRD) pattern (Fig. 1c) and average diameter of 9.1 ± 0.5 nm (Fig. 1d). The broad peaks at 25.1°, 41.6°, and 75.9° correspond to the (111), (220), and (422) crystal planes of the cubic AlSb, respectively (PDF 00-006-0233)²⁴. NCs have an absorption spectrum with a first excitonic peak at 377 nm and band-edge PL emission at 480 nm (Fig. 1e).

Principle of biointerface design and operation. The photovoltaic unit was fabricated by sequential planar deposition of zinc oxide (ZnO), P3HT, and AlSb NC layer onto indium tin oxide (ITO)-coated glass substrates (Fig. 1a). P3HT is used as the photoactive layer for light-triggered exciton generation due to their optical absorption in the visible spectral window, tunability of charge carrier density, and solution-processability³¹. Further, P3HT is one of the prototypical conjugated polymers used for neural interfaces³²⁻³⁶, showing high biocompatibility³³. Although the bioelectrical performance of P3HT could be further enhanced by the coupling with inorganic materials such as perovskite²³, ZnO¹⁷, lead sulfide (PbS)^{17,37}, and graphene³⁵, to the best of our knowledge no inorganic hole acceptor layer was reported for the P3HT layer due to its high level of conduction band (CB) at -5.1 eV²³. Advantageously, AlSb NC is a proper candidate to form a Type-II heterojunction with P3HT allowing for hole accumulation to NCs, respectively (Fig. 1b). Hence, after excitons are generated in P3HT, the accumulation of photogenerated holes between the electrode and electrolyte junction may restrict the Faradaic charge transfer due to their heavy effective mass ($m_h = 0.98m_e$ ²⁴). As the capacitive charge transfer is preferred due to its non-faradaic nature, the charge carriers that are localized on the interface need to have an energy level such that it would not cause any faradaic reaction. For this purpose, moving the electrons toward the ITO layer is preferred. In our design, the band alignment between the layers was arranged such that the holes accumulate to AlSb NC/electrolyte interface. There are two contributors to this accumulation: the use of hole blocking ZnO layer¹⁷, which is proven to be biocompatible in various forms³⁸, and AlSb NC having the highest occupied molecular orbital (HOMO) energy level of -4.6 eV higher than the P3HT HOMO level of -5.1 eV. Upon illumination, the photogenerated holes effectively routed to AlSb NC/electrolyte interface, which can attract negative ions and generate resulting negative capacitive currents, in other words, in the direction from biointerface to electrolyte during the onset of light. Therefore, instead of using electrons, in this study we used photogenerated holes for induction of capacitive currents.

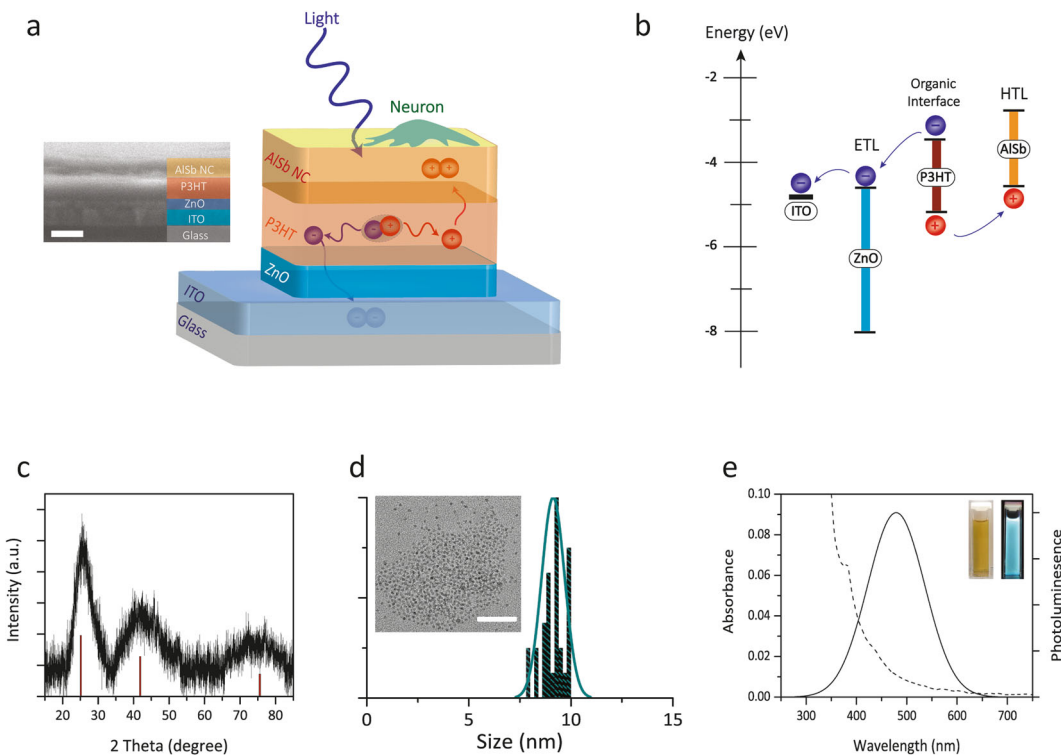


Fig. 1 Biointerface design and operation. **a** The structure of the photovoltaic biointerface using ITO, ZnO, P3HT, AlSb NCs as substrate, electron transport layer (ETL), donor component and hole transport layer (HTL), respectively. Inset: Cross-sectional scanning electron microscopy (SEM) image of the biointerface (Scale bar: 200 nm). **b** Energy levels of bulk ZnO⁵⁵, P3HT^{17,23}, and AlSb⁵⁵. **c** XRD pattern of the AlSb NCs. (The vertical lines at the bottom are the corresponding positions and intensities of X-ray reflections for the bulk AlSb (PDF 00-006-0233)²⁴). **d** Particle size distribution of the AlSb NCs (minimum 50 particles were counted). Inset: TEM image of the AlSb NC (Scale bar: 50 nm)). **e** Absorbance (dashed) and photoluminescence (solid) of the AlSb NCs dispersed in toluene. (Photograph of the AlSb NC solution under ambient (left inset) and UV light (right inset)).

Photocurrent measurement. We investigated photocurrent and photovoltage of ITO/ZnO/P3HT/AlSb (biointerface) and ITO/ZnO/P3HT (control) structures, respectively. A three electrode photoelectrochemical characterization setup in a modified artificial cerebrospinal fluid (modified aCSF), mimicking the biological environment, was used for chronopotentiometry and chronocomperometry measurements under red and blue light illumination (Fig. 2a). To understand the effect of AlSb NCs, initially photoresponse of the control and biointerface were tested under red-light centered at 630 nm, which is longer than the AlSb NC absorbance cut-off wavelengths (Fig. 1e) and within the absorption band of P3HT³⁹. The photovoltage and photocurrent levels are enhanced for the control and biointerface with only ~6% and ~5% increase, respectively, due to the enhanced surface roughness of electrical double layer (Fig. 2b, c). Hence, the measurements under the red illumination revealed that AlSb NC has a small contribution to the photoresponse of the biointerface above its absorbance cut-off wavelengths. Moreover, Faradaic contribution ~1% indicates a highly capacitive charge injection process (Fig. 2d). Next, 445 nm blue light-emitting diode (LED) illumination was used to excite AlSb NCs, and the generated photovoltage increases from 52 mV cm⁻² to 98 mV cm⁻² (Fig. 2b) corresponding to an ~80% increase in comparison with the control. At the same time, the biointerface can inject a capacitive current of ~0.6 mA cm⁻² with suppressed Faradaic contribution of 1.4%, which is 2.3-fold higher than the control (Fig. 2c, d). Hence, this shows that the light-triggered hole generation at the utmost surface layer interfacing with electrolyte significantly improves the photovoltage and photocurrent.

Moreover, the photocurrent transient advantageously revealed fast charging (~1 ms) and discharging (~2.7 ms) phases (Fig. 2d),

and the rise time was measured as ~55 μ s. The fast charge injection kinetics of the biointerface can be used for high-frequency neural stimulation. The short rise times of photocurrent and photovoltage indicate the charge generation is based on capacitive processes rather than photothermal or Faradaic effects. The biointerface showed higher photocurrent peaks than the control device under different illumination intensities with a mean of 2.4-fold increase (Fig. 2e). Another important criterion for neuronal stimulators is the total injected charge that causes the voltage changes in the cell membrane¹⁹. By integrating the photocurrent transient²⁰, charge injection amount was calculated. AlSb NCs increased the total charge injection by a mean of 30% with respect to the control device and it corresponds to 0.19 μ C cm⁻² under 445 nm, 100 mW cm⁻² illumination (Fig. 2f), which is at the level of required charge threshold for retinal stimulation⁴⁰. The charge carried in the ON and OFF phases (Fig. 3c) is calculated as $0.191 \pm 0.031 \mu$ C cm⁻² and $0.173 \pm 0.029 \mu$ C cm⁻², respectively, corresponding to $9.4 \pm 0.4\%$ difference (mean \pm s.e.m., $n=6$). To test the charge conservation, we integrated the photocurrent transient starting from the beginning of the stimulation until $T=10\tau \gg \tau$ after the end of the stimulus⁴¹. For each measurement the dark current was measured and the current after stimulation is adjusted to remove that offset⁴¹. The total integrated charge is calculated as $1.766 \pm 0.156 \text{ nC cm}^{-2}$, which is 0.92% of the charge injection during the ON phase of the stimulus and indicates a highly capacitive charge injection process.

To test its potential for single cell stimulation, a second set of photocurrent experiments were carried out by using a patch-clamp electrophysiology system. As we proved the contribution of AlSb NC under exciting different wavelengths by photo-

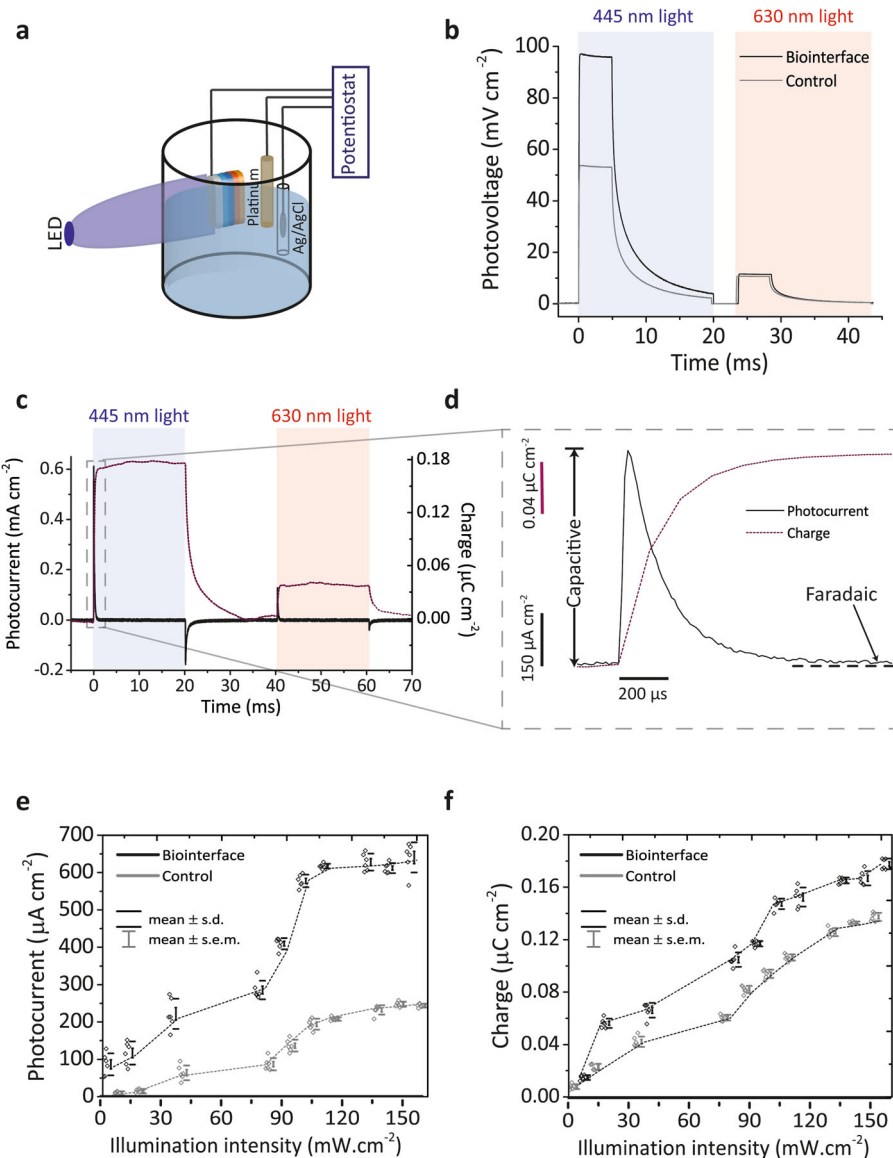


Fig. 2 Optoelectronic responses with AlSb NCs using photoelectrochemical measurements. **a** Schematic of photoelectrochemical measurement system. A potentiostat module combined with platinum and Ag/AgCl electrodes was utilized for the measurement. The working electrode was directly connected to the ITO layer with a metal clip as the return electrode in the system. The device area of $\sim 1\text{ cm}^2$ was illuminated and modified artificial cerebrospinal fluid was used as the supporting solution. **b** Photovoltage transient response under the illumination of 445 nm and 630 nm light pulses with trains of 20 ms, 100 mW cm⁻². Blue and red semi-transparent areas show the 445 nm and 630 nm light illumination periods, respectively. **c** Photocurrent transient response (black) and charge evolution (purple) under the same conditions as **b**. The gray dashed box marks the region that is shown in **d**. **d** Close-up for the best photocurrent performance under blue light illumination (445 nm) to identify the rise time, capacitive and Faradaic components of the photocurrent response. **e** Photocurrent and **f** charge amounts generated by control (gray) and biointerface (black) under different illumination intensities of 20 ms, 445 nm pulses (means \pm s.e.m., means \pm s.d., $n = 6$).

electrochemical measurements, patch-clamp experiments were conducted for 445 nm LED light illumination with trains of 20 ms light pulses. To mimic the working condition in biological media, we operated without any wired ground connected to the biointerfaces, but only used the amplifier ground immersed in the electrolyte (Fig. 3a). The photoresponse of the biointerface showed only 109 pA (3.7%) of Faradaic photocurrent contribution by long-lasting currents¹⁴ indicating again a highly capacitive charge injection process (Fig. 3b). Similarly, by using the electrophysiology setup AlSb NCs improve the photocurrent of the biointerface by a mean of 1.6-fold, even under the low intensity light $<100\text{ mW cm}^{-2}$ (Fig. 3c). To further explore the charge injection dependence on light intensity, photocurrent

transient was again integrated for different illumination powers ranging from 10 mW cm^{-2} to 150 mW cm^{-2} . Under each illumination power, the biointerface showed higher charge injection than the control device and can generate more than 8 pC of charge over 120 mW cm^{-2} (Fig. 3d). This amount of total charge injection is sufficient to evoke action potential on primary mammalian neurons^{42,43}, for example, voltage-gated ion channel openings were seen to elicit action potential by the injection of $\sim 8\text{ pC}$ ¹⁶ charge. Hence, AlSb NCs can facilitate the delivery of necessary amount of charges for stimulation of neurons. As control experiments, bare glass, glass:ITO, and glass:ITO/ZnO substrates were measured and the maximum measured photocurrent is less than 0.12 nA, which is much less than the

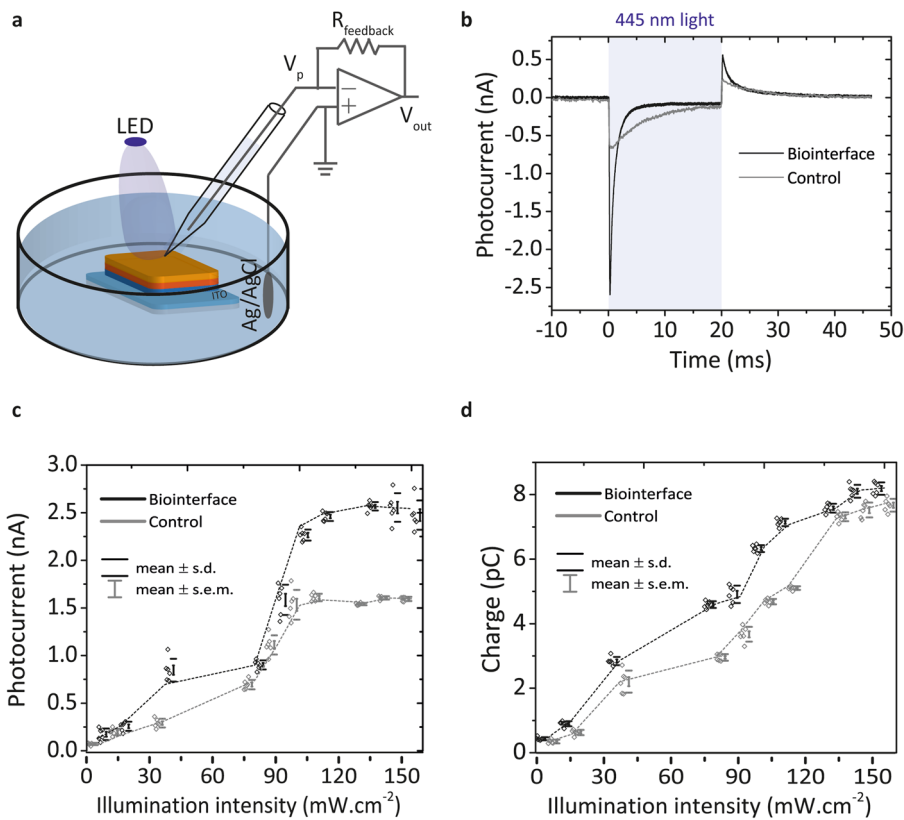


Fig. 3 Optoelectronic responses with AlSb NCs by using patch-clamp measurement system. **a** Schematic of the patch-clamp photocurrent measurement system. The glass pipette was positioned close to the surface of the biointerface and control device ($<5\text{ }\mu\text{m}$). ITO layer was in direct contact with electrolyte to be used as the return electrode. **b** Photocurrent response upon illumination with trains of 20 ms, 100 mW cm^{-2} , 2 Hz light pulses for control (gray) and biointerface (black). Blue semi-transparent area shows the 445 nm light illumination period. **c** Photocurrent and **d** charge injection amounts under different illumination intensities (means \pm s.e.m., means \pm s.d., $n = 6$).

photocurrent peak of the biointerface (2.5 nA) under the same stimulation condition (Supplementary Fig. 1). Moreover, the photocurrent gradient was measured by increasing distances from the center of the illumination spot toward outside of the beam (Supplementary Fig. 2). The photocurrent decrease toward outside of the illumination spot suggests that charge accumulation and corresponding stimulation are confined to the illumination spot³³.

Photostability and biocompatibility tests. We tested stability and biological safety of the biointerface. For the photostability test, the performance of the biointerface was characterized under cyclic and continuous illumination¹⁴. The photocurrent peak was measured for 2000 cycles of blue-light illumination. The results indicated high photocurrent retention by $81 \pm 2.36\%$ (mean \pm s.d., $n = 6$) of the biointerface (Fig. 4a). During the cyclic photostability tests, we calculated the ratio of sustained photocurrent amplitude over the photocurrent peak. This ratio should increase over the cycles if faradaic processes are significant in the system. However, the ratio did not change significantly over the cycles (Supplementary Fig. 3). Therefore, this result in addition to total charge calculations in photocurrent experiments suggest the charge injection is highly capacitive with negligible faradaic contribution^{14,41}. Continuous illumination test was carried out for 20 h under constant 100 mW cm^{-2} and we observed photocurrent retention by $76 \pm 1.96\%$ (mean \pm s.d., $n = 6$).

To explore the effect of sterilization, which is an essential step towards in vitro and in vivo studies, AlSb NC coated biointerfaces were sterilized with low-temperature hydrogen peroxide (H_2O_2) plasma⁴⁴. The chronopotentiometry measurements indicate that

our biointerface showed robust performance after sterilization by high retention of photovoltage generation by $93.7 \pm 1.17\%$ (mean \pm s.d., $n = 3$). Moreover, to evaluate the functional biointerface lifetime, a passive accelerated ageing test^{45,46} was performed at $87\text{ }^\circ\text{C}$ in a dry oven under dark conditions. The biointerfaces were placed in a glass petri-dish filled with physiological saline solution (0.9% NaCl, pH 7.4) that corresponds to the acceleration factor of 32⁴⁶, which can be calculated by *acceleration factor* (f) = $2^{\Delta t/10}$ where $\Delta t = 87\text{ }^\circ\text{C} - 37\text{ }^\circ\text{C}$ assuming body temperature of $37\text{ }^\circ\text{C}$. We chose $87\text{ }^\circ\text{C}$ both to provide an acceleration factor of 32 and also as a reasonable temperature that saline solution can be sustained. During each accelerated ageing session of 68 h, corresponding to 3 months, we measured the photovoltage generation by chronopotentiometry measurements. The ageing test was performed for 810 h corresponding to 36 months and indicates robust device performance for at least 3 years (Fig. 4b). Furthermore, cell viability measurements using 3-(4,5-dimethylthiazol-2-yl)-2,5-diphenyl tetrazolium bromide (MTT) were performed to examine the biocompatibility of the AlSb integrated biointerface. Primary hippocampal neurons were cultured on the biointerface and the biointerface did not induce any significant effect on cell viability and morphology on primary neurons (Fig. 4c, d, Supplementary Fig. 4, Supplementary Movies 1 and 2).

Light-induced capacitive neural stimulation. We measured the photoresponse of the primary hippocampal neurons cultured on glass:ITO/ZnO/P3HT/AlSb NC biointerface, and also glass:ITO/ZnO/P3HT control device and glass:ITO control device as control groups. A patch-clamp recording system was utilized without any

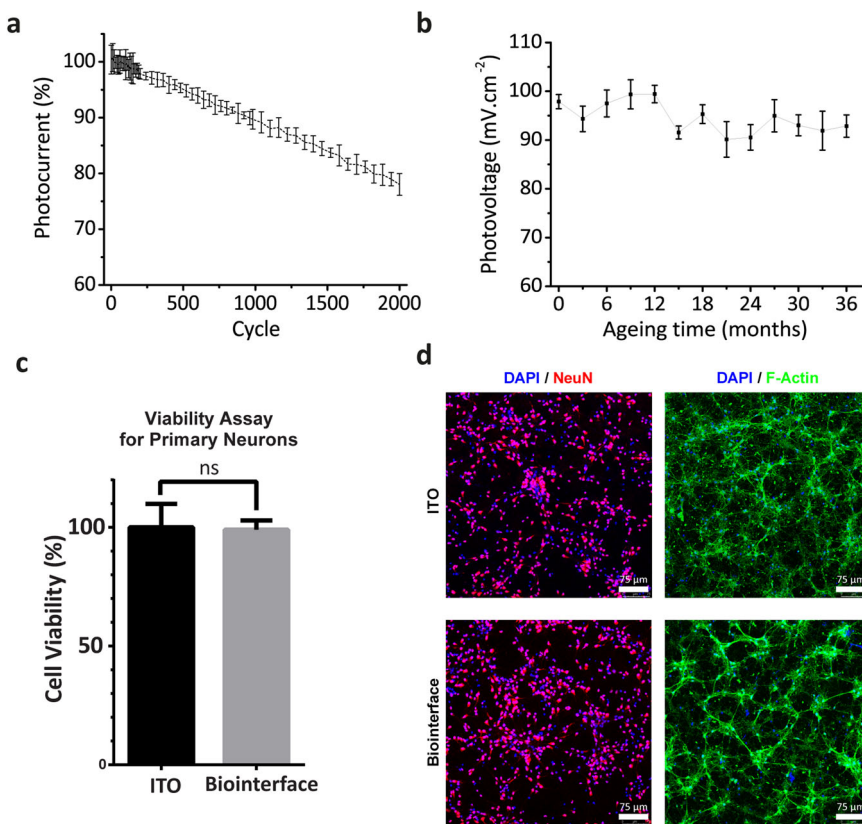


Fig. 4 Device stability and biocompatibility in vitro. **a** Cyclic photostability of the biointerface. Photocurrent peaks were measured in periodic cyclic illumination and measurements were normalized to analyze cyclic stability. Blue LED at the nominal wavelength of 445 nm with the frequency of 2 Hz, pulse width of 20 ms, and intensity of 100 mW cm^{-2} was used. **b** Chronopotentiometry measurements during passive accelerated ageing test to reveal photovoltage generation performance. Biointerfaces were placed in physiological saline solution at 87°C in dry oven under dark conditions for 810 h to simulate the ageing for 36 months. Chronopotentiometry measurements were repeated in each 68 h (mean \pm s.d., $n = 6$). **c** The effect of the biointerface on metabolic activity of primary hippocampal neurons was examined by MTT viability assay and compared with ITO control. An unpaired two-tailed *t*-test was performed to determine the level of significance. Each experiment was carried out with at least four biological replicates (mean \pm s.d., $n = 4$). $*p < 0.05$ was considered as statistically significant, and nonsignificant differences are presented as “ns”. **d** Immunofluorescence images of primary hippocampal neurons on the biointerface and ITO controls. Primary hippocampal neurons co-stained with DAPI (blue), Anti-NeuN (red), and Anti-F-actin (green) (scale bar: 75 μm).

applied bias current to study changes in intracellular membrane potential with respect to a distant Ag/AgCl reference electrode (Fig. 5a). During all measurements, cells adhered onto the biointerfaces and the I-V curve of the cells under dark condition were measured.

For the light excitation, we used trains of 20 ms, 50 mW cm^{-2} , 445 nm blue LED illumination with changing frequencies of 1, 2, 5, 10, and 20 Hz. We observed that 1, 2, 5, and 10 Hz stimulation effectively induce action potential (Fig. 5b, c, d) with $>90\%$ success rate and reduces only to $\sim 73\%$ for 20 Hz (Fig. 5e) ($n = 20$). Moreover, we calculated the mean (\pm s.e.m.) latency³³ with respect to the spike peak to the stimulation onset and also the jitter as the standard deviation of latencies measured over all neurons (Fig. 5g and Supplementary Fig. 5) and the AlSb NC based biointerface has a short mean latency of 16.70 ± 0.478 ms and a mean jitter of 1.748 ± 0.120 ms ($n = 20$)⁴⁷.

During electrophysiology experiments with primary hippocampal neurons on AlSb biointerface and on ITO control substrates, we measured the resting membrane potential before and after the optical stimulation (Fig. 5f and Supplementary Fig. 6). Light stimulation was ineffective for neurons cultured on ITO control substrates. Moreover, the resting membrane potential on the biointerface and ITO control substrates did not show any significant difference (measurements before optical

stimulation, Student's *t*-test, $P = 0.0848$, $n = 20$; measurements after 1 min optical stimulation with 20 ms pulses at 2 Hz, Student's *t*-test, $P = 0.1822$, $n = 20$), which indicates no significant adverse effect on cell electrophysiology³³. To understand the resolution of the biointerface 1 Hz, 20 ms, 50 mW cm^{-2} , 445 nm, $\sim 600 \mu\text{m}$ diameter LED pulses were applied, and neural activity was recorded while moving away the center of the illumination spot from the targeted neuron ($n = 4$). This experiment revealed that moving the stimulation source $\sim 225 \mu\text{m}$ away from the targeted cell reduces successful spike rate by 50%, and after $\sim 325 \mu\text{m}$ we did not observe any successful stimulation (Supplementary Fig. 7). Secondly, after being $\sim 775 \mu\text{m}$ away from the targeted neuron, the biointerface cannot induce any membrane potential change. Furthermore, to study the photothermal contribution and provide an upper boundary on temperature changes, we utilized the thermodynamic relation¹⁷ for 50 mW, 1 s light pulses (Supplementary Note 1). The temperature change of 0.364°C shows the photothermal effects are negligible⁴⁸. Also, the resting membrane potential measurements before and after the 1 min stimulation did not show any significant difference, which also supports negligible photothermal effects.

Although biocompatibility experiments suggest a safe design in terms of consisting materials, retinal prosthesis require

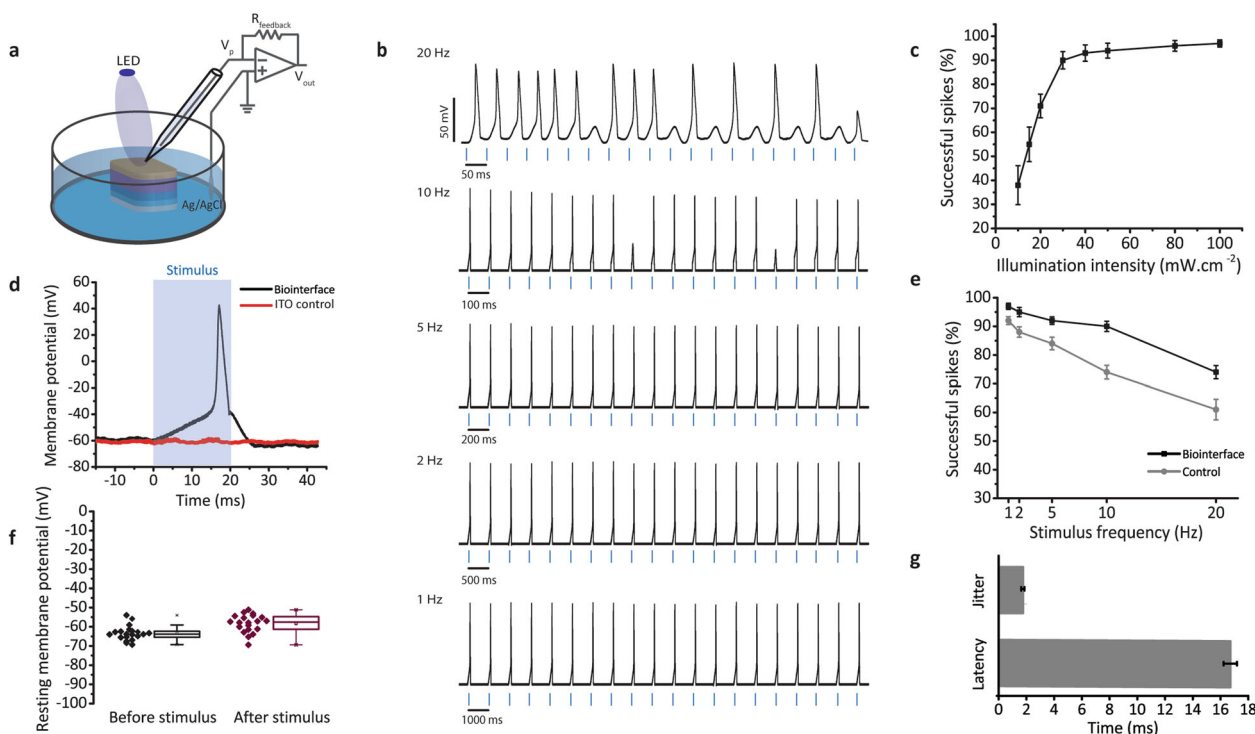


Fig. 5 Neural photostimulation in vitro. **a** Electrophysiology patch-clamp measurement setup. The illumination source is a blue LED with the central wavelength of 445 nm. **b** Neural activity of primary hippocampal neurons cultured on the biointerface in response to a train of 20 pulses (20 ms, 50 mW cm^{-2} at 1, 2, 5, 10, 20 Hz). Blue bars represent the start of the pulses. **c** Successful spike ratio under different illumination intensities. 20 pulses of 20 ms at 1 Hz were applied in various intensities ($n = 20$, mean \pm s.d.). **d** Intracellular membrane potential change with respect to a distant Ag/AgCl electrode was measured after the photostimulation of primary hippocampal neurons on the glass:ITO control (red) and the biointerface (black) under illumination of 100 mW cm^{-2} with 20 ms illumination pulses. Blue semi-transparent area shows the 445 nm light illumination period. **e** Successful spike ratio of neurons on the glass:ITO/ZnO/P3HT control (gray) and the biointerface (black) under different illumination frequencies of 20 ms, 50 mW cm^{-2} , 20 pulses ($n = 20$, mean \pm s.d.). **f** The resting membrane potential of neurons on biointerface were measured before and after 1 min optical stimulation with 20 ms pulses at 2 Hz ($n = 20$, mean \pm s.e.m.). **g** The mean latency with respect to the spike peak to the stimulation onset and also the jitter as the standard deviation of latencies for all neurons ($n = 20$, mean \pm s.e.m.).

functionality within the light intensity limits of ocular safety. The maximum permissible chronic radiant exposure (MPH_c) is limited by the lowest intensity due to single-pulse, thermal, and photochemical limits⁴⁹. Since our biointerface facilitates pulsed stimulation, ocular safety is also considered for repetitive pulses and photochemical damage provides the limiting factor⁵⁰ of $\text{MPH}_c = 54 \text{ mW cm}^{-2}$. Advantageously, our biointerface is functional to elicit action potential even under light intensities as low as 10 mW cm^{-2} , and shows high stimulation success under $30\text{--}50 \text{ mW cm}^{-2}$ illumination, which is lower than the ocular safety limit^{49,50}.

Discussion

Herein, we demonstrated AlSb nanocrystal based biointerface for photostimulation of neurons. For that a Type-II AlSb and P3HT heterojunction is formed that led the movement of electrons to the ITO through the hole blocker ZnO layer and accumulation of holes to the AlSb nanocrystals that can function without cadmium (Cd) and mercury (Hg) content. To date, the biointerfaces using nanoparticles of HgTe³, CdTe⁸, and CdSe/CdS⁵¹ showed depolarization and hyperpolarization capabilities on various cell lines. However, the previous biointerfaces were suffered from the required high intensity illumination, electrochemical cellular coupling, or unstable action potential generation. Moreover, in previous reports, biocompatibility and long-term stability had not been studied extensively, and for capacitive charge injection, the band energy levels for these nanoparticles are not compatible with most of

the organic polymers. Compared with these reports, AlSb NCs, which is just introduced in 2019²⁴, enabled the most efficient and safe neural stimulator among the nanocrystal-based ones, operating under light intensities lower than the ocular safety limits^{49,50}. Since the biointerface provides capacitive currents, our design showed high photostability over 36 months operational lifetime in aqueous environment, and stable photo-response under cyclic/continuous illumination. AlSb NC integrated biointerface shows high biocompatibility at in vitro applications. Moreover, AlSb has proper energy levels to be integrated with several other organic polymers such as PCBM³⁷ and PTB7-Th⁵² for further studies. AlSb has an indirect bulk band gap of 1.58 eV that correspond to a band edge in near-IR⁵³. Thus, engineering of AlSb nanocrystals hold also significant potential for future retinal prosthetics against age macular degeneration like PRIMA communicating with the photovoltaic unit at near-IR for restoration of vision⁵⁴.

This study shows the high potential of colloidal nanocrystals that can bring forward new opportunities for biointerfaces. There is plenty of room at the nanocrystals for opto-bioelectronics that can originate from their unique optoelectronic and electrochemical properties, which can be tuned by size, shape, composition, and ligands. Our results pointed out that novel forms of semiconductor nanocrystals like AlSb can facilitate not only safe and high-performance nanoengineered neural interfaces, but also have the potential to be integrated in various architectures to meet the need of the charge transport requirements of electrical cellular interfacing.

Methods

Synthesis of AlSb NCs. AlSb NCs were synthesized according to our previous study²⁴. The final NCs were dispersed in toluene and the concentration was adjusted to 20 mg ml⁻¹.

Characterization of AlSb NCs. UV–Vis absorption and photoluminescence (PL) were carried out using Edinburgh Instruments FS5 spectrophotometer. Standard quartz cuvettes with the cross dimensions of 1 cm × 1 cm were used and the emission and excitation bandwidths were set as 3 nm and 2 nm, respectively. For the TEM analysis, FEI Talos F200S by an accelerating voltage of 200 keV was used and specimens were prepared by depositing directly a holey carbon film on a copper support grid. For the XRD analysis, layers of NC solution in toluene were drop-cast and dried on a glass substrate and analyzed with Bruker D2 Phaser X-ray diffractometer a with Cu K_α radiation ($\lambda = 1.541 \text{ \AA}$).

Biointerface fabrication. Photoelectrodes were fabricated onto the glass substrates, which were covered with unpatterned indium tin oxide (ITO) (Ossila, S111). The substrate cleaning procedure consists of sonication in NaOH solution for 5 min, in tension-active agent mixed with deionized water solution (HELMANEX II, 3%) for 15 min, in deionized water for 15 min, in pure acetone for 5 min, and finally in isopropyl alcohol for 5 min all at 55 °C. The cleaned substrates were treated with UV–ozone for 20 min to eliminate any other possible residues on the ITO surface. For photoactive layer, P3HT (95.7% regioregular) (>99% pure, Ossilla) was utilized without any further purification. Photoactive solution was prepared as an 18.75 mg ml⁻¹ solution of P3HT in o-dichlorobenzene, stirred for overnight at 70 °C. For ZnO layer coating, ZnO precursor solution was prepared by mixing 219.3 mg zinc acetate dehydrate (Zn(CH₃CO₂)₂·2H₂O) from Sigma-Aldrich in 2 ml of 2-methoxyethanol (C₃H₈O₂) and 90 mg of ethanolamine (HOCH₂CH₂NH₂) and sonicated for 25 min at 50 °C. Then, the ZnO solution was filtered by a 0.45 µm PVDF filter. ZnO layer was spin coated onto the ITO substrates at 2000 rpm for 60 s and annealed at 280 °C for 15 min. P3HT layer was fabricated onto ZnO layer by spin coating at 1500 rpm for 90 s and annealed at 150 °C for 10 min. For the AlSb layer, AlSb solution in toluene with the concentration of 20 mg ml⁻¹ was used. AlSb layer was coated on ZnO at 2000 rpm for 60 s using and annealed at 150 °C for 10 min to eliminate the residual solvent. The cross-sectional SEM image, taken by Zeiss ultra plus field emission scanning electron microscope, indicates a 115 nm thick AlSb layer.

Chronoamperometry and chronopotentiometry measurements. For the electrochemical experiments, we used an Autolab Potentiostat Galvanostat PGSTAT (Metrohm, Netherlands). The three-electrode configuration utilizes Ag/AgCl as the reference electrode, platinum wire as the counter electrode, and connection to the biointerface as the working electrode. All measurements were carried out in a modified aCSF medium as the electrolyte solution at the room temperature. The device was excited with blue and red LEDs. The optical power was controlled with an optical power meter (Newport 843-R). The data was analyzed using the NOVA software.

Photocurrent measurements. The measurements were carried out using Olympus T2 upright microscope and extracellular patch clamp (EPC) 800 patch clamp amplifier (HEKA Elektronik GmbH, Pfalz, Germany). The modified aCSF aqueous medium was prepared by mixing 10 mM of 4-(2-hydroxyethyl)-1-piperazineethanesulfonic acid (HEPES), 10 mM of glucose, 2 mM CaCl₂, 140 mM of NaCl, 1 mM of MgCl₂, 3 mM of KC, and mixed with the distilled water. The pH was calibrated to 7.4 using 1 M NaOH. As the illumination source, Thorlabs' blue (M450LP1) was used. LED system was driven by DC2200 - High-Power 1-Channel LED Driver with Pulse Modulation (Thorlabs Inc, NJ, USA). Photocurrent was measured without electrical grounding the ITO layer, and the ground is connected to the electrolyte solution to simulate the biological environment.

Ethical usage of animals. All animal manipulation and experimental procedures have been approved by the Institutional Animal Care and Use Committees of Koç University (Approval No: 2019.HADYEK.023) according to Directive 2010/63/EU of the European Parliament and of the Council On Protection of Animals Used for Scientific Purposes and the Republic of Turkey 5199 Animal Protection Law, Article 9 and 17. All animal experiments in the study are carrying out with the responsible veterinarian and the researchers who have the certificate for experimental animal usage.

Primary hippocampal neuron isolation and culture. Hippocampal regions were extracted from decapitated E15–E17 Wistar Albino rats and were placed immediately in ice-cold Hank's Balanced Salt Solution (HBSS, Thermo Fisher Scientific, MA, USA). The hippocampi were incubated in 0.25% Trypsin-EDTA solution (Thermo Fisher Scientific, MA, USA) with 2% DNase-I supplement (NeoFroxx, Einhausen, Germany) for 20 min in a 37 °C incubator. Then the cells were centrifuged and the supernatant was changed with Dulbecco's Modified Eagle Medium/Nutrient Mixture F-12 (DMEM/F12 Thermo Fisher Scientific, MA, USA) supplemented with 10% fetal bovine serum (FBS, Heat Inactivated, GE Healthcare,

IL, USA) and 1% penicillin/streptomycin (Thermo Fisher Scientific, MA, USA). DMEM/F12 was removed and Neurobasal Medium (NBM, Thermo Fisher Scientific, MA, USA) supplemented with B27, L-glutamine, β-mercaptoethanol, glutamate (Thermo Fisher Scientific, MA, USA) was added to the cell pellet. The cells were triturated and were passed through a 70 µm cell strainer. The homogenous cell solution was seeded in poly-D-lysine (PDL, Sigma-Aldrich, MO, USA) coated substrates. After a 3-day incubation of cells on substrates in a 37 °C incubator with 5% carbon dioxide, the media of the cells on substrates were changed with NBM supplemented with cytosine arabinoside (Sigma-Aldrich, MO, USA) to inhibit growth of glial cells. After 24-hour incubation with cytosine arabinoside, the media were changed with NBM. Primary hippocampal neurons on the substrates were maintained at 37 °C in a 5% CO₂, 85% humidified incubator until used for experiments.

In vitro biocompatibility test. To analyze the cell viability of primary hippocampal neurons on AlSb integrated devices, MTT assay was used. The neural growth medium was prepared using Neurobasal Medium (NBM, Thermo Fisher Scientific, MA, USA) supplemented with B27, L-glutamine, β-mercaptoethanol, glutamate (Thermo Fisher Scientific, MA, USA), and penicillin–streptomycin (Gibco 15240-062). The device was sterilized first by cleaning with 70% ethanol followed by air-drying. The surface was further sterilized under UV irradiation for 30 min. The substrates were placed in 6-well plates. The primary hippocampal neurons were isolated and cultured (3 × 10⁵ cells per well) on the substrates in 85% humidified incubator at 37 °C with 5% CO₂. After 48 h of incubation, the medium was replaced with 1 ml of 5 mg ml⁻¹ MTT (Thermo Fisher Scientific, MA, USA) in PBS solution and 4 ml of NBM mixture per well. After that, the cells were incubated at 37 °C and 5% CO₂ atmosphere for an additional 4 h. The medium was vacuumed from each well and substrates were transferred to an empty 6-well plate. In each well, 1:1 mixture of DMSO and ethanol was added to dissolve the formazan crystals. The solution was transferred to a 96-well plate and the absorbance was measured at 600 nm (for background) and at 690 nm (for absorbance) with Synergy H1Micro-plate Reader (Bio-Tek Instruments, VT, USA). The relative cell viability was calculated as follows: viability = (OD_{sample}/OD_{control}) × 100. The optical density (OD) of the sample was obtained from the cells grown on a photoelectrode, and the OD of control was obtained from the cells grown on the ITO substrates.

Immunofluorescence staining and imaging. Primary hippocampal neurons (2.5 × 10⁵ cells per sample) were seeded as explained above on ITO control substrate and the biointerface and incubated for 48 h at 37 °C in cell culture incubator. After incubation, primary neurons were fixed by 4% paraformaldehyde and washed three times with PBS-T (Phosphate Buffered Saline, 0.1% Triton X-100). Cells were blocked in PBS solution containing 5% BSA (Bovine Serum Albumin) and 0.1% Triton X-100. Primary hippocampal neuron samples were incubated with rabbit anti NeuN antibody (ab177487, Abcam, Cambridge, UK) overnight and washed three times with PBS-T. Then, primary hippocampal neuron samples were incubated with goat anti-rabbit IgG H&L Alexa Fluor 555(4413, Cell Signaling Technology, MA, USA) for fluorophore marking of anti-NeuN primary antibody for 90 min at 37 °C. For visualization of the cytoskeleton, primary neuron samples also were incubated with FITC-conjugated phalloidin antibody (Sigma-Aldrich, P5282) for 90 min at 37 °C. All samples were washed three times with PBS-T, then mounted with DAPI supplemented mounting medium (ab104139, Abcam, Cambridge, UK) to observe nuclei. Finally, immunofluorescence imaging was done using confocal fluorescence microscope (TCS SP8 DLS, Leica, Wetzlar, Germany).

Electrophysiology experiments. Experiments were performed by EPC 800 patch clamp amplifier (HEKA Elektronik GmbH, Pfalz, Germany). The AlSb integrated and control devices were cleaned with 70 vol% ethanol solution and incubated for 3 days in DI water. The pulled patch pipettes of 4–6 MΩ were utilized to carry out the whole-cell patch clamp experiment. Extracellular medium (modified aCSF) was prepared as mentioned in the photocurrent measurement section. The internal cellular medium was prepared by mixing 140 mM KCl, 2 mM MgCl₂, 10 mM HEPES, 10 mM ethylene glycol-bis(β-aminoethyl ether)-N,N,N',N'-tetraacetic acid (EGTA), 2 mM Mg-ATP in water and the pH was calibrated to 7.2–7.3 using 1 M KOH. Patch pipettes were filled with the intracellular solution to achieve whole-cell patch. A digital camera integrated Olympus T2 upright microscope was used to patch and monitor the cells. The blue LED (M450LP1, Thorlabs Inc, NJ, USA) was used as the light source. LED system was driven by DC2200 - High-Power 1-Channel LED Driver with Pulse Modulation (Thorlabs Inc, NJ, USA).

Ocular safety limits. Following the limits for safe use of lasers by 2014 American National Standards Institute (ANSI)⁵⁰, we calculated limiting factor for maximum permissible chronic radiant exposure⁴⁹ (MPH_c) for evenly spaced pulsed illumination using provided computer implementation⁵⁰. Among the damaging limits, single pulse limit, MPH_c = 1737 mW cm⁻², average-power thermal limit, MPH_c = 897 mW cm⁻², average-power photochemical limit, MPH_c = 54 mW cm⁻² and repetitive-pulse limit, MPH_c = 695 mW cm⁻² were calculated. We assumed the focal length of the eye $f = 20$ mm, $\alpha = 5$ mrad visual angle and illumination with 445 nm, 20 Hz, 20 ms pulses.

Reporting summary. Further information on research design is available in the Nature Research Reporting Summary linked to this article.

Data availability

The datasets that support all the findings of this study are available from the corresponding authors upon reasonable request.

Received: 11 June 2020; Accepted: 26 January 2021;

Published online: 19 February 2021

References

- Parameswaran, R. et al. Photoelectrochemical modulation of neuronal activity with free-standing coaxial silicon nanowires. *Nat. Nanotechnol.* **13**, 260 (2018).
- Wang, Y. & Guo, L. Nanomaterial-enabled neural stimulation. *Front. Neurosci.* **10**, 1–7 (2016).
- Pappas, T. C. et al. Nanoscale engineering of a cellular interface with semiconductor nanoparticle films for photoelectric stimulation of neurons. *Nano Lett.* **7**, 513–519 (2007).
- Efros, A. L. et al. Evaluating the potential of using quantum dots for monitoring electrical signals in neurons. *Nat. Nanotechnol.* **13**, 278–288 (2018).
- Bahmani Jalali, H. et al. Exciton recycling via InP quantum dot funnels for luminescent solar concentrators. *Nano Res.* **12**, 1–7 (2020).
- Kagan, C. R., Lifshitz, E., Sargent, E. H. & Talapin, D. V. Building devices from colloidal quantum dots. *Science.* **353**, 5–7 (2016).
- Karatum, O. et al. Light-emitting devices based on type-II InP/ZnO quantum dots. *ACS Photonics* **6**, 939–946 (2019).
- Lugo, K., Miao, X., Rieke, F. & Lin, L. Y. Remote switching of cellular activity and cell signaling using light in conjunction with quantum dots. *Biomed. Opt. Express* **3**, 447–454 (2012).
- Molokanova, E. et al. Quantum dots move beyond fluorescence imaging the unique properties of quantum dots allow them to be optimized for voltage sensing and for light-controlled electrical activation of cells. *Biophotonics Int.* **15**, 26 (2008).
- Derfus, A. M., Chan, W. C. W. & Bhatia, S. N. Probing the cytotoxicity of semiconductor quantum dots. *Nano Lett.* **4**, 11–18 (2004).
- Bahmani Jalali, H. et al. Biocompatible quantum funnels for neural photostimulation. *Nano Lett.* **19**, 5975–5981 (2019).
- Bahmani Jalali, H. et al. Effective neural photostimulation using indium-based type-II quantum dots. *ACS Nano* **12**, 8104–8114 (2018).
- Merrill, D. R., Bikson, M. & Jefferys, J. G. R. Electrical stimulation of excitable tissue: design of efficacious and safe protocols. *J. Neurosci. Methods* **141**, 171–198 (2005).
- Jiang, Y. et al. Rational design of silicon structures for optically controlled multiscale biointerfaces. *Nat. Biomed. Eng.* **2**, 508 (2018).
- Bareket-Keren, L. & Hanein, Y. Novel interfaces for light directed neuronal stimulation: advances and challenges. *Int. J. Nanomed.* **9**, 65 (2014).
- Abdullaeva, O. S. et al. Organic photovoltaic sensors for photocapacitive stimulation of voltage-gated ion channels in neuroblastoma cells. *Adv. Funct. Mater.* **29**, 1805177 (2019).
- Srivastava, S. B. et al. Band alignment engineers faradaic and capacitive photostimulation of neurons without surface modification. *Phys. Rev. Appl.* **11**, 12 (2019).
- Rivnay, J., Wang, H., Fenno, L., Deisseroth, K. & Malliaras, G. G. Next-generation probes, particles, and proteins for neural interfacing. *Sci. Adv.* **3**, e1601649 (2017).
- Cogan, S. F. Neural stimulation and recording electrodes. *Annu. Rev. Biomed. Eng.* **10**, 275–309 (2008).
- Han, M. et al. Organic photovoltaic pseudocapacitors for neurostimulation. *ACS Appl. Mater. Interfaces* **12**, 42997–43008 (2020).
- Shamsi, J., Urban, A. S., Imran, M., De Trizio, L. & Manna, L. Metal halide perovskite nanocrystals: synthesis, post-synthesis modifications, and their optical properties. *Chem. Rev.* **119**, 3296–3348 (2019).
- Li, X. et al. All inorganic halide perovskites nanosystem: synthesis, structural features, optical properties and optoelectronic applications. *Small* **13**, 1603996 (2017).
- Aria, M. M. et al. Perovskite-based optoelectronic biointerfaces for non-bias-assisted photostimulation of cells. *Adv. Mater. Interfaces* **6**, 1900758 (2019).
- Bahmani Jalali, H. et al. Colloidal aluminum antimonide quantum dots. *Chem. Mater.* **31**, 4743–4747 (2019).
- Adachi, S. & Adachi, S. *Optical Constants of Crystalline and Amorphous Semiconductors* (Springer, 1999).
- Barate, D., Teissier, R., Wang, Y. & Baranov, A. N. Short wavelength intersubband emission from InAs/AlSb quantum cascade structures. *Appl. Phys. Lett.* **87**, 51103 (2005).
- Linnebach, R. & Benz, K. W. Bridgman growth of AlSb. *J. Cryst. Growth* **53**, 579–585 (1981).
- Johnson, J. E. Aluminum antimonide thin films by coevaporation of the elements. *J. Appl. Phys.* **36**, 3193–3195 (1965).
- Schwartz, G. P., Gualtieri, G. J., Sunder, W. A. & Farrow, L. A. Light scattering from quantum confined and interface optical vibrational modes in strained-layer GaSb/AlSb superlattices. *Phys. Rev. B* **36**, 4868 (1987).
- Glaser, E. R., Kennedy, T. A., Bennett, B. R. & Shanabrook, B. V. Strong emission from As monolayers in AlSb. *Phys. Rev. B* **59**, 2240–2244 (1999).
- Green, R. & Abidian, M. R. Conducting polymers for neural prosthetic and neural interface applications. *Adv. Mater.* **27**, 7620–7637 (2015).
- Benfenati, V. et al. Photostimulation of whole-cell conductance in primary rat neocortical astrocytes mediated by organic semiconducting thin films. *Adv. Healthc. Mater.* **3**, 392–399 (2014).
- Ghezzi, D. et al. A polymer optoelectronic interface restores light sensitivity in blind rat retinas. *Nat. Photonics* **7**, 400–406 (2013).
- Gautam, V., Rand, D., Hanein, Y. & Narayan, K. S. A polymer optoelectronic interface provides visual cues to a blind retina. *Adv. Mater.* **26**, 1751–1756 (2014).
- DiFrancesco, M. L. et al. A hybrid P3HT-graphene interface for efficient photostimulation of neurons. *Carbon N. Y.* **162**, 308–317 (2020).
- Ghezzi, D. et al. A hybrid bioorganic interface for neuronal photoactivation. *Nat. Commun.* **2**, 166 (2011).
- Srivastava, S. B. et al. Efficient photocapacitors via ternary hybrid photovoltaic optimization for photostimulation of neurons. *Biomed. Opt. Express* **11**, 5237 (2020).
- Dagdeviren, C. et al. Transient, biocompatible electronics and energy harvesters based on ZnO. *Small* **9**, 3398–3404 (2013).
- Fei, Z. et al. Influence of backbone fluorination in regioregular poly(3-alkyl-4-fluoro) thiophenes. *J. Am. Chem. Soc.* **137**, 6866–6879 (2015).
- Zhang, M., Tang, Z., Liu, X. & Van der Spiegel, J. Electronic neural interfaces. *Nat. Electron.* **3**, 191–200 (2020).
- Derek, V., Rand, D., Migliaccio, L., Hanein, Y. & Glowacki, E. D. Untangling photofaradaic and photocapacitive effects in organic optoelectronic stimulation devices. *Front. Bioeng. Biotechnol.* **8**, 1–8 (2020).
- Rand, D. et al. Direct electrical neurostimulation with organic pigment photocapacitors. *Adv. Mater.* **30**, 1707292 (2018).
- Maya-Vetencourt, J. F. et al. A fully organic retinal prosthesis restores vision in a rat model of degenerative blindness. *Nat. Mater.* **16**, 681–689 (2017).
- Rutala, W. A., Gergen, M. F. & Weber, D. J. Comparative evaluation of the sporicidal activity of new low-temperature sterilization technologies: ethylene oxide, 2 plasma sterilization systems, and liquid peracetic acid. *Am. J. Infect. Control* **26**, 393–398 (1998).
- Lu, S. et al. Accelerated discovery of stable lead-free hybrid organic-inorganic perovskites via machine learning. *Nat. Commun.* **9**, 1–8 (2018).
- Ferlauto, L. et al. Design and validation of a foldable and photovoltaic wide-field epiretinal prosthesis. *Nat. Commun.* **9**, 1–15 (2018).
- Airaghi Leccardi, M. J. I. et al. Photovoltaic organic interface for neuronal stimulation in the near-infrared. *Commun. Mater.* **1**, 21 (2020).
- Martino, N. et al. Photothermal cellular stimulation in functional bio-polymer interfaces. *Sci. Rep.* **5**, 1–8 (2015).
- Delori, F. C., Webb, R. H. & Sliney, D. H. Maximum permissible exposures for ocular safety (ANSI 2000), with emphasis on ophthalmic devices. *J. Opt. Soc. Am. A* **24**, 1250 (2007).
- Yan, B., Vakulenko, M., Min, S. H., Hauswirth, W. W. & Nirenberg, S. Maintaining ocular safety with light exposure, focusing on devices for optogenetic stimulation. *Vision Res.* **121**, 57–71 (2016).
- Bareket, L. et al. Semiconductor nanorod–carbon nanotube biomimetic films for wire-free photostimulation of blind retinas. *Nano Lett.* **14**, 6685–6692 (2014).
- Melikov, R. et al. Plasmon-coupled photocapacitor neuromodulators. *ACS Appl. Mater. Interfaces* **12**, 35940–35949 (2020).
- Paufler, P. Landolt-Börnstein. Numerical data and functional relationships in science and technology. New Series. Group III: Crystal and Solid State Physics. Vol. 22: Semiconductors. Subvolume a: Intrinsic Properties of Group IV Elements and III-V, II-VI and I-VII Compounds. Ed. by O. Madelung Springer-Verlag Berlin-Heidelberg-New York-London-Paris-Tokyo 1987. XII + 451 pp. Hard cover DM 1120.—, ISBN 3-540-16609-2. *Cryst. Res. Technol.* **23**, 1360–1360 (1988).
- Palanker, D., Le Mer, Y., Mohand-Said, S., Muqit, M. & Sahel, J. A. *Ophthalmology* Vol. 127 (Elsevier Inc., 2020).
- Van de Walle, C. G. & Neugebauer, J. Universal alignment of hydrogen levels in semiconductors, insulators and solutions. *Nature* **423**, 626–628 (2003).

Acknowledgements

This project has received funding from the European Research Council (ERC) under the European Union's Horizon 2020 Research and Innovation Programme (grant agreement no. 639846). S.N. also acknowledges the support by the Turkish Academy of Sciences

(TÜBA-GEBIP; The Young Scientist Award Program) and the Science Academy of Turkey (BAGEP; The Young Scientist Award Program). The authors gratefully acknowledge use of the services and facilities of the Koç University Research Center for Translational Medicine (KUTTAM), funded by the Republic of Turkey Ministry of Development. The content is solely the responsibility of the authors and does not necessarily represent the official views of the Ministry of Development. The authors thank Shashi Bhushan Srivastava for his assistance in chronopotentiometry and chronocomperometry measurements, Sina Khoshshima and Baris Yagci for SEM images at KUYTAM (Koc University Surface Science and Technology Center).

Author contributions

M.H. planned experiments, fabricated biointerfaces, performed photostimulation, photoelectrochemical and electrophysiological experiments, analyzed the data, and wrote the manuscript. H.B.J. planned experiments, synthesized and characterized the AlSb NCs, fabricated biointerfaces, analyzed the data, and wrote the manuscript. E.Y. prepared primary hippocampal neuron cultures, performed cell viability assays, immunofluorescence staining experiments, analyzed data, and wrote the manuscript. M.H.Q. acquired immunofluorescence confocal images of *in vitro* experiments, assisted to primary hippocampal neuron cultures. A.S. interpreted and discussed the data and supervised primary hippocampal neuron culture, cell viability assays, and fluorescence microscopy experiments. S.N. planned and supervised the entire study, and wrote the manuscript. All the authors read and accepted the manuscript.

Competing interests

The authors declare no competing interests.

Additional information

Supplementary information The online version contains supplementary material available at <https://doi.org/10.1038/s43246-021-00123-4>.

Correspondence and requests for materials should be addressed to S.N.

Peer review information Primary handling editor: John Plummer

Reprints and permission information is available at <http://www.nature.com/reprints>

Publisher's note Springer Nature remains neutral with regard to jurisdictional claims in published maps and institutional affiliations.



Open Access This article is licensed under a Creative Commons Attribution 4.0 International License, which permits use, sharing, adaptation, distribution and reproduction in any medium or format, as long as you give appropriate credit to the original author(s) and the source, provide a link to the Creative Commons license, and indicate if changes were made. The images or other third party material in this article are included in the article's Creative Commons license, unless indicated otherwise in a credit line to the material. If material is not included in the article's Creative Commons license and your intended use is not permitted by statutory regulation or exceeds the permitted use, you will need to obtain permission directly from the copyright holder. To view a copy of this license, visit <http://creativecommons.org/licenses/by/4.0/>.

© The Author(s) 2021